Proposed approximation for contact angles in Shan-and-Chen-type multicomponent multiphase lattice Boltzmann models

Haibo Huang,[1] Daniel T. Thorne, Jr.,[2] Marcel G. Schaap,[3] and Michael C. Sukop[1]
[1]*Department of Earth Sciences, Florida International University, Miami, Florida 33199, USA*
[2]*Department of Math, Physics and Computer Science, Georgetown College, Georgetown, Kentucky 40324, USA*
[3]*Department of Soil, Water and Environmental Science, University of Arizona, Tucson, Arizona 85721, USA*
(Received 19 February 2007; revised manuscript received 20 August 2007; published 3 December 2007)

We propose a method for approximating the adhesion parameters in the Shan and Chen multicomponent, multiphase lattice Boltzmann model that leads to the desired fluid-solid contact angle. The method is a straightforward application of Young's equation with substitution of the Shan and Chen cohesion parameter and a density factor for the fluid-fluid interfacial tension, and the adhesion parameters for the corresponding fluid-solid interfacial tensions.

DOI: 10.1103/PhysRevE.76.066701 PACS number(s): 47.11.−j, 05.20.Dd, 68.03.Cd, 68.08.Bc

I. INTRODUCTION

Wetting and spreading phenomena of fluids on solid phases are important to many industrial and natural processes [1]. When an immiscible droplet comes into contact with a solid phase, there is a contact line between the wetting and nonwetting fluids and the solid surface. The contact angle between the fluids and the surface can be calculated through Young's equation provided the interfacial tensions between the fluid components and between each component and the solid surface are known [2,3].

Numerical methods can be very instrumental in enhancing understanding of fluid behavior in complex systems, such as porous media. The lattice Boltzmann method (LBM), which is based on mesoscopic kinetic equations, is a popular and numerically robust technique for simulating single and multiphase fluids in arbitrarily complex media [4–9]. Although the fluid dynamical characteristics of the LBM are well understood analytically and the method has been successfully applied in the study of wetting and spreading phenomena involving interfacial dynamics [4–10], there are still uncertainties in the interactions between the lattice Boltzmann fluid and the solid phase. Progress has been made for several LBM model types. For example, Briant *et al.* [1] investigated the wetting and spreading phenomena for single component multi-phase fluids using the free-energy-based LBM. Latva-Kokko and Rothman [11] derived an estimate of the contact angle as a function of a wetting tendency of the wall when using color-gradient-based LBM. However, the multicomponent multiphase LBM proposed by Shan and Chen (SC) [4] is a more popular multiphase model and is better defined in terms of interparticle potential than the color-gradient based LBM [12] and we will focus on it exclusively here.

There have been many studies on wetting and spreading phenomena using the SC model. Martys and Chen [6] studied multicomponent fluids in complex three-dimensional geometries. In their simulations, the interaction force between a fluid and a wall was introduced. They found that reasonably well-defined contact angles could be obtained by adjusting the interaction strength between each fluid and a surface such that one of the fluids wets the surface. Using the SC LBM, Schaap *et al.* [13] and Pan *et al.* [9] studied the displacement of immiscible fluids in different porous media and estimated adhesion parameters through empirical calibration methods. In the above studies [6,9,13], no explicit relationship between contact angle and adhesion parameter has been proposed. Kang *et al.* [7,14] studied displacement of immiscible droplets subject to gravitational forces in a two-dimensional (2D) channel and a three-dimensional (3D) duct. In their studies, the contact angles considered ranged from only 60° to 120° and the relationship between adhesion parameters and contact angles was estimated as linear.

Benzi *et al.* [15] presented a mesoscopic model for the interaction between a solid wall and a *single component* multiphase fluid (e.g., [16]). They derived an analytical expression for the contact angle that covers the range of contact angles from 0° to 180° but depends on prior knowledge of the ρ profiles, and hence is not useful as a predictive tool. Our focus here is on the multicomponent multiphase SC model.

To the best of our knowledge, all previous work on determining contact angles from adhesion parameters in the SC multicomponent, multiphase lattice Boltzmann model is strictly empirical and limited to a relatively small range of contact angles. The details of the methods used to measure contact angles were not provided in previous work. In this paper, we present an algorithm for contact angle measurement that allows systematic, consistent measurements. Then we use measurements of simulated drops to develop and empirically verify an expression based on Young's equation for determining adhesion parameters that lead to the desired fluid-solid contact angle in the SC LBM.

II. METHOD

A. Shan-and-Chen-type multicomponent multiphase LBM

Here we implement the SC LBM [4] in two and three dimensions for a multicomponent multiphase system. In the model, one distribution function is introduced for each of the two fluid components. Each distribution function represents a fluid component and satisfies the following lattice Boltzmann equation:

$$f_a^\sigma(\mathbf{x}+\mathbf{e}_a\Delta t, t+\Delta t) = f_a^\sigma(\mathbf{x},t) - \frac{\Delta t}{\tau_\sigma}[f_a^\sigma(\mathbf{x},t) - f_a^{\sigma,\mathrm{eq}}(\mathbf{x},t)], \tag{1}$$

where $f_a^\sigma(\mathbf{x},t)$ is the σth component density distribution function in the ath velocity direction, and τ_σ is a relaxation time which is related to the kinematic viscosity as $\nu_\sigma = c_s^2(\tau_\sigma - 0.5\Delta t)$. The equilibrium distribution function $f_a^{\sigma,\mathrm{eq}}(\mathbf{x},t)$ can be calculated as

$$f_a^{\sigma,\mathrm{eq}}(\mathbf{x},t) = w_a\rho_\sigma\left[1 + \frac{\mathbf{e}_a\cdot\mathbf{u}_\sigma^{\mathrm{eq}}}{c_s^2} + \frac{(\mathbf{e}_a\cdot\mathbf{u}_\sigma^{\mathrm{eq}})^2}{2c_s^4} - \frac{\mathbf{u}_\sigma^{\mathrm{eq}^2}}{2c_s^2}\right]. \tag{2}$$

In Eqs. (1) and (2), the $\mathbf{e}_a$'s are the discrete velocities. For the D2Q9 model, they are given by

$$[\mathbf{e}_0,\mathbf{e}_1,\mathbf{e}_2,\mathbf{e}_3,\mathbf{e}_4,\mathbf{e}_5,\mathbf{e}_6,\mathbf{e}_7,\mathbf{e}_8] = c\begin{bmatrix} 0 & 1 & 0 & -1 & 0 & 1 & -1 & -1 & 1 \\ 0 & 0 & 1 & 0 & -1 & 1 & 1 & -1 & -1 \end{bmatrix}.$$

For the D3Q19 model, the discrete velocities are given by

$$[\mathbf{e}_0,\mathbf{e}_1,\mathbf{e}_2,\mathbf{e}_3,\mathbf{e}_4,\mathbf{e}_5,\mathbf{e}_6,\mathbf{e}_7,\mathbf{e}_8,\mathbf{e}_9,\mathbf{e}_{10},\mathbf{e}_{11},\mathbf{e}_{12},\mathbf{e}_{13},\mathbf{e}_{14},\mathbf{e}_{15}\mathbf{e}_{16},\mathbf{e}_{17},\mathbf{e}_{18}]$$
$$= c\begin{bmatrix} 0 & 1 & -1 & 0 & 0 & 0 & 0 & 1 & 1 & -1 & -1 & 1 & -1 & 1 & -1 & 0 & 0 & 0 & 0 \\ 0 & 0 & 0 & 1 & -1 & 0 & 0 & 1 & -1 & 1 & -1 & 0 & 0 & 0 & 0 & 1 & 1 & -1 & -1 \\ 0 & 0 & 0 & 0 & 0 & 1 & -1 & 0 & 0 & 0 & 0 & 1 & 1 & -1 & -1 & 1 & -1 & 1 & -1 \end{bmatrix}.$$

In Eq. (2), for the D2Q9 model, $w_a = 4/9$ $(a=0)$, $w_a = 1/9$ $(a=1,2,3,4)$, $w_a = 1/36$ $(a=5,6,7,8)$, and for the D3Q19 model, $w_a = 1/3$ $(a=0)$, $w_a = 1/18$ $(a=1,2,\ldots,6)$, $w_a = 1/36$ $(a=7,8,\ldots,18)$, $c_s = c/\sqrt{3}$, where $c = \Delta x/\Delta t$ is the ratio of lattice spacing Δx and time step Δt. Here, we define one lattice unit (Δx) as 1 l.u. In Eq. (2), ρ_σ is the density of the σth component, which can be obtained from $\rho_\sigma = \Sigma_a f_a^\sigma$.

The macroscopic velocity $\mathbf{u}_\sigma^{\mathrm{eq}}$ is given by

$$\mathbf{u}_\sigma^{\mathrm{eq}} = \mathbf{u}' + \frac{\tau_\sigma \mathbf{F}_\sigma}{\rho_\sigma}, \tag{3}$$

where $\mathbf{u}'$ is a velocity common to the various components defined as

$$\mathbf{u}' = \frac{\sum_\sigma \left(\sum_a \frac{f_a^\sigma \mathbf{e}_a}{\tau_\sigma}\right)}{\left(\sum_\sigma \frac{\rho_\sigma}{\tau_\sigma}\right)}. \tag{4}$$

In Eq. (3), $\mathbf{F}_\sigma = \mathbf{F}_{c,\sigma} + \mathbf{F}_{\mathrm{ads},\sigma}$ is the force acting on the σth component, here including fluid-fluid cohesion $\mathbf{F}_{c,\sigma}$ and fluid-solid adhesion $\mathbf{F}_{\mathrm{ads},\sigma}$.

Each node in the computational domain is occupied by every σ component though one is dominant under most conditions as described below. The minor components can be thought of as dissolved within the dominant component. With the techniques used here, the overall density of fluid in the domain is approximately uniform because the densities are complementary in the sense that $\Sigma_\sigma \rho_\sigma = \rho_i$ (the constant initial density) or $\rho_1 + \rho_2 = \rho_i$ in a two-fluid system.

B. Fluid-fluid cohesion and fluid-solid adhesion

The cohesive force acting on the σth component is defined as [6]

$$\mathbf{F}_{c,\sigma}(\mathbf{x},t) = -G_c\rho_\sigma(\mathbf{x},t)\sum_a w_a\rho_{\bar\sigma}(\mathbf{x}+\mathbf{e}_a\Delta t,t)\mathbf{e}_a, \tag{5}$$

where the σ and $\bar\sigma$ denote two different fluid components and G_c is a parameter that controls the strength of the cohesion force.

The surface force acting on the σth component can be computed as follows [6]:

$$\mathbf{F}_{\mathrm{ads},\sigma}(\mathbf{x},t) = -G_{\mathrm{ads},\sigma}\rho_\sigma(\mathbf{x},t)\sum_a w_a s(\mathbf{x}+\mathbf{e}_a\Delta t)\mathbf{e}_a. \tag{6}$$

Here $s(\mathbf{x}+\mathbf{e}_a\Delta t)$ is an indicator function that is equal to 1 or 0 for a solid or a fluid domain node, respectively. The interaction strength between each fluid and a wall can be adjusted by the parameters $G_{\mathrm{ads},\sigma}$. Most previous literature has suggested that $G_{\mathrm{ads},\sigma}$ should be positive for nonwetting fluid and negative for wetting fluid [6,7,9].

C. Young's equation

Young's equation for computing the contact angle contains interfacial tension values between the two fluids (σ_{12}) and between each fluid and the surface (σ_{S1} and σ_{S2}):

$$\cos\theta_1 = \frac{\sigma_{S2} - \sigma_{S1}}{\sigma_{12}}. \tag{7}$$

This equation determines the contact angle θ_1 measured in fluid 1 (Fig. 1) [17].

D. Application of Young's equation to multicomponent multiphase LBM

Here we propose a straightforward application of Young's equation with substitution of the LBM cohesion parameter and a density factor $G_c[(\rho_1-\rho_2)/2]$ for the fluid-fluid inter-

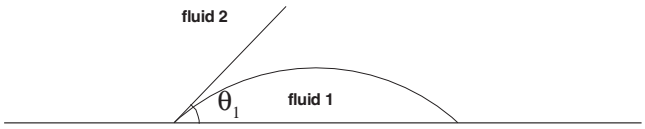

FIG. 1. Contact angle.

facial tension, and the adhesion parameters $G_{ads,1}$, $G_{ads,2}$ from Eq. (6) for the corresponding fluid-solid interfacial tensions:

$$\cos\theta_1 = \frac{G_{ads,2} - G_{ads,1}}{G_c \frac{\rho_1 - \rho_2}{2}}. \quad (8)$$

Equation (8) is simple and able to determine the contact angle using only the parameters G_c, the equilibrium main density ρ_1, and the associated dissolved density ρ_2, which can be determined as discussed in the following section, and $G_{ads,1}$ and $G_{ads,2}$. Equation (8) is similar to an equation proposed in [16] but is significantly improved since it gives more accurate predictions.

E. Determining G_c and the surface tension

In the SC model the parameter G_c controls the fluid-fluid interfacial tension and there is a threshold value $G_{c,crit}=1/(\rho_1+\rho_2)$ for G_c [6] beyond which an initially uniform mixed system of two immiscible fluids will yield a stable separation. ρ_1 and ρ_2 are the main and dissolved densities of fluid 1 and fluid 2, respectively. The critical value $G_{c,crit}=1.0$ for $\rho_1+\rho_2=1$. To verify this we carried out two series of 2D simulations where we placed a pure bubble of fluid 1 (ρ_1) inside a 100×100 square of fluid 2 (ρ_2) with periodic boundaries; both fluids had equal total masses (i.e., the number of pixels occupied by fluid 1 was equal to that of fluid 2). The two simulation series had initial densities of $\rho_i=2$ and 8 (where $\rho_i=\rho_1+\rho_2$) and the parameter G_c was varied from zero until numerical instabilities occurred. Figure 2 shows the density of fluid 1 (ρ_1) and a smaller dissolved density of fluid 2 (ρ_2) inside the bubble, scaled according to initial density. From the figure, we can see that for $0\leq G_c\rho_i\leq 1.0$ the scaled densities are 0.5 for each component because the two fluids diffuse until a homogeneous solution is present at equilibrium. When $G_c\rho_i>1.0$, the bubble filled with fluid 1 becomes increasingly "pure" with the density of fluid 1 eventually exceeding 1 for $G_c\rho_i>1.8$ due to the compressibility of the fluid. For a various $G_c\rho_i$ values, the equilibrium ρ_1 and associated dissolved ρ_2 can be determined from Fig. 2.

TABLE I. Adhesion parameters and contact angles (degrees) for fluid 1 ($G_c=0.9$ and $G_{ads,1}=-G_{ads,2}$).

Case	$G_{ads,2}$	Contact angle computed from Eq. (8)	Contact angle measured from Fig. 3
a	−0.4	156.4	158.3
b	−0.3	133.4	135.1
c	−0.2	117.3	117.0
d	−0.1	103.2	103.2
e	0.1	76.8	75.3
f	0.2	62.7	59.5
g	0.3	46.6	40.6
h	0.4	23.6	18.9

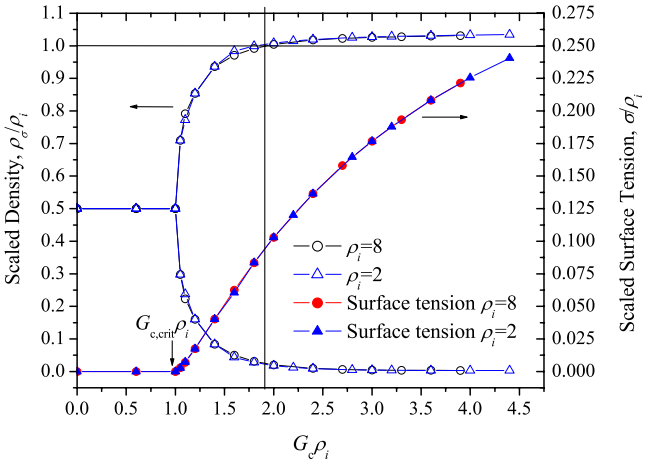

FIG. 2. (Color online) Scaled component densities (left-hand *y* axis) and scaled lattice surface tension (right-hand *y* axis) as a function of the scaled cohesion parameter, $G_c\rho_i$. The simulations were carried out for two initial densities. The vertical line depicts the $G_c\rho_i$ value used in the rest of the study. $G_{c,crit}\rho_i$ depicts the critical $G_c\rho_i$ value above which stable phase separation is possible (see text).

The pressure at position $\mathbf{x}$ can be determined from the densities as $p(\mathbf{x})=[\rho_1(\mathbf{x})+\rho_2(\mathbf{x})]/3+G_c\rho_1(\mathbf{x})\rho_2(\mathbf{x})/3$ [7,18]. By measuring the component densities inside and outside a drop or bubble, the interfacial tension σ can be determined through Laplace's law $p(\mathbf{x}_{inside})-p(\mathbf{x}_{outside})=\sigma/R$, where R is the radius of the bubble. The scaled surface tension as a function of $G_c\rho_i$ is also illustrated in Fig. 2. The relationship between σ and $G_c\rho_i$ is approximately linear when $1.0<G_c\rho_i<2.0$.

G_c should be chosen carefully. Larger G_c is preferable for multiphase simulations because it increases the interface

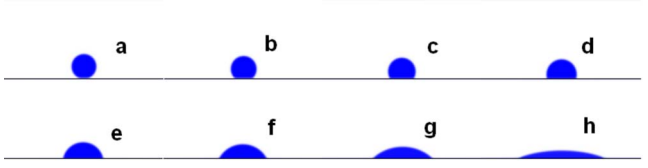

FIG. 3. (Color online) Simulations of different contact angles for multicomponent fluids interacting with a surface (parameters G_c, $G_{ads,1}$, $G_{ads,2}$ and measured contact angles for each case are listed in Table I). The density of the first substance is shown in dark gray. Simulation domain is 200×100 l.u.^{2}. Images represent 24 000 time steps from an initial condition of a 41×20 l.u.^{2} rectangle of the first substance surrounded by the second substance. In each region, the substances have density 2 and dissolved density 0.06. $\tau=1$ time step for both fluids.

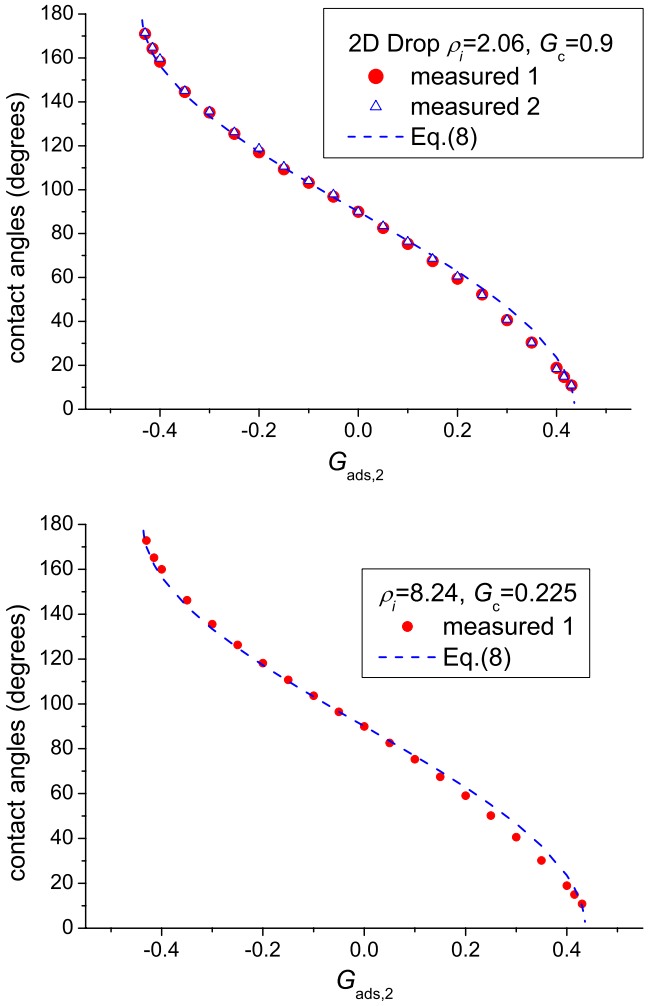

FIG. 4. (Color online) Contact angles for two fluids interacting with a surface vs the value of the adhesion parameter, $G_{ads,2}$ ($G_{ads,1}=-G_{ads,2}$). Simulation domain is 200×100 l.u.^{2}. Results represent 24 000 time steps from an initial condition of a 41×20 l.u.^{2} ("measured 1") and a 41×40 l.u.^{2} ("measured 2") rectangle of the first substance surrounded by the second substance. (Left subfigure: In each region, the substances have density 2 and dissolved density 0.06. Right subfigure: In each region, the substances have density 8 and dissolved density 0.24.) $\tau=1$ time step for both fluids.

sharpness and limits the "solubility" of the fluids within each other. On the other hand, smaller G_c is preferable because that alleviates some numerical difficulties and can reduce the compressibility of LBM fluids [13]. From Fig. 2, we found that $1.6<G_c\rho_i<2.0$ is an appropriate compromise. Here we chose $G_c\rho_i=1.8$.

Although the determination of equilibrium densities in Fig. 2 is obtained from cases where both fluids have equal masses and the domains have periodic boundary conditions, Fig. 2 is also valid for cases where the two fluids have different initial masses and for the presence of a solid boundary.

To demonstrate this, we prepared the following example. We initialize a small rectangular area (e.g., 4% of the whole 200×100 domain) near a wall with substance 1 surrounded by substance 2, and in each region, the substances have density 2.0 and dissolved density 0.6 (this dissolved density is arbitrary and an order of magnitude larger than the expected equilibrium dissolved density for "main" density of ~2). In the simulation we set $G_c\rho_i=1.8$, where $\rho_i=2.0+0.6=2.6$, $G_c=0.6923$, $G_{ads1}=-0.318$, and $G_{ads2}=0.318$.

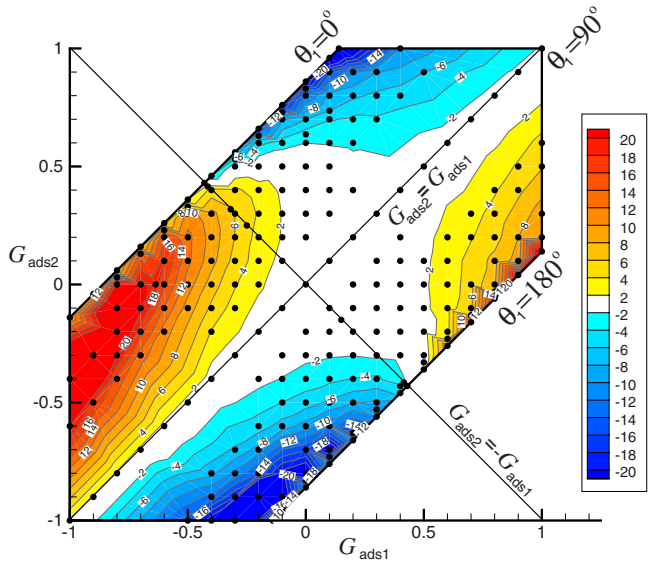

FIG. 5. (Color online) Difference (in degrees) between contact angle computed using Eq. (8) and contact angle measured using algorithm described in text as a function of $G_{ads,1}$ and $G_{ads,2}$ ($G_c=0.9$). Black dots show parameter values used in simulations.

We observe that in all regions (except the interface area), the equilibrium main fluid density is 2.565 and dissolved density is 0.086, which agrees well with Fig. 2 because for $G_c\rho_i=1.8$, $\rho_{main}/\rho_{dissolved}=2.565/0.086$ is about $1/0.03$.

We also simulated other cases with different initial masses, G_{ads1}, and G_{ads2}. In the equilibrium state, the ratio of the main fluid density and dissolved density all agree well with the data in Fig. 2.

Finally, we considered cases with densities far from the expected equilibrium condition. If the main substances in all regions have for example, initial density 8.0 and dissolved density 0.00, then the equilibrium area of substance 1 will be smaller than its initialized area, but the contact angle can still be well-predicted provided we use the equilibrium density values.

As an example, we initialized all regions with main density 8 and dissolved density 0.0, with $G_c=0.225$. After 90 000 time steps, the equilibrium $\rho_{main}/\rho_{dissolved}=7.80/0.24$ agrees well with Fig. 2.

These simulations confirm that Fig. 2 can be directly used in Eq. (8) to give a desired contact angle *a priori*.

III. RESULTS

A. Contact angle measurement

Contact angles can be computed from measurements of the base and height of drops on a surface. If the base and height of a droplet are L and H, respectively, the radius of the droplet can by calculated from $R=(4H^2+L^2)/8H$. Then, the

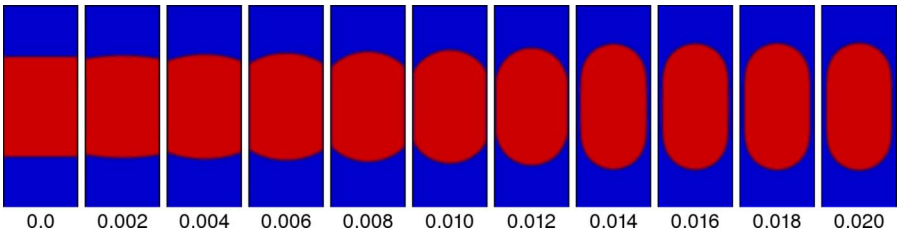

FIG. 6. (Color online) Simulations of wetting (dark gray, fluid 1) and nonwetting (light gray, fluid 2) fluids in a $38\times38\times78$ l.u.^{3} duct [13]. The interface curvature becomes more intense and the contact angle for a nonwetting drop increases from 90° to 180° as $G_{\mathrm{ads},2}$ increases from 0.0 to 0.020 as indicated in the figure. $G_c=0.025$.

measured contact angle can be obtained through the formula $\tan\theta_1=L/2/(R-H)$. The measurement of base and height involves some ambiguities that require resolution or at least a consistent approach.

The main difficulties in measuring drop base and height is how to define a precise location of the interface between the drop and the ambient fluid, since the simulated interface is actually several lattice units thick. Here we chose a cutoff density value as $\rho_{\mathrm{cut}}=0.5\rho_A$, where ρ_A is the density of the fluid that forms the drop. It is obvious that choosing ρ_{cut} too close to ρ_A or its associated dissolved density should be avoided since those values occur far from the center of the interface. Using linear interpolation method, we determined the drop base width and the height of drop. Then we used the preceding formulas to determine the contact angle in a simulation.

B. Verification of proposed equation

To verify the proposed method for determining the contact angles, some 2D and 3D numerical simulations were carried out and 2D and 3D results from the literature [13,14] were reevaluated. First, multicomponent fluids interacting with a surface were studied. A sampling of parameters $G_{\mathrm{ads},1}$ and $G_{\mathrm{ads},2}$ that we used to compute different contact angles with Eq. (8) is listed in Table I. The results are illustrated in Fig. 3. The density of the first substance is shown in dark gray. Images represent 24 000 time steps from an initial condition of a 41×20 l.u.^{2} rectangle of the first substance surrounded by the second substance. In each region, the substances have density 2 and dissolved density 0.06, which can be obtained from Fig. 2.

Figure 4 shows the measured contact angles as a function of $G_{\mathrm{ads},2}$ when $G_{\mathrm{ads},1}=-G_{\mathrm{ads},2}$. The contact angles that are obtained from Eq. (8) are also shown for comparison. The contact angles calculated with Eq. (8) agree well with the measured ones over most of the range.

These results suggest that the prediction of Eq. (8) becomes somewhat less accurate at low contact angle. This prompted us to investigate the range of applicability of Eq. (8). Figure 5 shows that there are large ranges of the parameters $G_{\mathrm{ads},1}$ and $G_{\mathrm{ads},2}$ where there is only a small difference between the contact angle computed using Eq. (8) and contact angle measured using the algorithm described previously. In particular, the difference is less than 2° in the white area of Fig. 5. Due to force imbalances, it is not surprising that the differences in predicted and observed contact angles become large where the difference in the magnitudes of the G_{ads} is large; for example, $G_{\mathrm{ads},1}=-0.7$ and $G_{\mathrm{ads},2}=0$ or $G_{\mathrm{ads},1}=0$ and $G_{\mathrm{ads},2}=-0.8$. Despite this, the best parameter sets do not appear to fall along the line $G_{\mathrm{ads},2}=-G_{\mathrm{ads},1}$ but rather along $G_{\mathrm{ads},2}\approx-G_{\mathrm{ads},1}+0.1$. The reasons for this apparent asymmetry are unclear and deserve further investigation, but the results provide good guidance for the selection of reliable parameter sets. It is interesting to note that, in accordance with Eq. (8), it is the difference in the G_{ads} values rather than their signs that determines the contact angle. For example, for both parameter sets $G_{\mathrm{ads},1}=0.1$ and $G_{\mathrm{ads},2}=-0.2$, and $G_{\mathrm{ads},1}=0.4$ and $G_{\mathrm{ads},2}=0.1$, the contact angle is 110.

Next, results from the literature were revaluated in terms of our proposed expression [Eq. (8)]. Schaap *et al.* [13] studied the contact angles of multicomponent fluids in 3D. The computational domain for the 3D capillary geometry [13] is a duct of length 78 l.u. and square cross section ranging from 8×8 to 38×38 l.u.^{2}. The nonwetting fluid was placed in the middle of the capillary with wetting fluid on top and bottom, and the total masses of wetting (first fluid) and nonwetting (second fluid) were equal.

In the study, $G_{\mathrm{ads},2}$ was varied between 0 and 0.02 with $G_c=0.025$ and $G_{\mathrm{ads},1}=-G_{\mathrm{ads},2}$. It should be noted that the definition of cohesion force in [13] is different from that in the present work. When G_c is defined on the basis of Eq. (5), the G_c of [13] would be 0.9 and both $G_{\mathrm{ads},2}$ and $G_{\mathrm{ads},1}$ would also 36 times larger than they are in [13]. The simulations were run to 100 000 time steps when equilibrium was nearly attained. The images in Fig. 6 represent vertical slices through the center of a 3D duct of size $38\times38\times78$ l.u.^{3}. These results show that the contact angle of the nonwetting drop changed from 90° at $G_{\mathrm{ads},2}=0$ to 180° at $G_{\mathrm{ads},2}\sim0.012$. At larger values of $G_{\mathrm{ads},2}$, the nonwetting fluid detaches from the wall and an increasingly thicker film of wetting fluid forms between the wall and the nonwetting fluid drop [13].

Figure 7 shows the contact angle as a function of $G_{\mathrm{ads},2}$ in the 3D simulations of [13] for various duct sizes. Although there are small discrepancies between Schaap's LBM results and our formula, the trend of the numerical results is highly consistent with the curve [Eq. (8)]. There appears to be a slight dependence of the contact angle on the duct size with the results for larger ducts approaching Eq. (8) more closely. We attribute this to the difficulties of accurately determining contact angle in small systems.

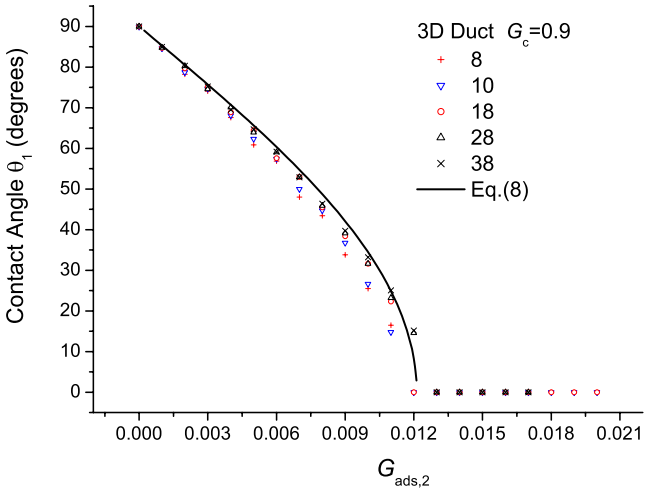

FIG. 7. (Color online) Contact angles of wetting fluid (fluid 1) in 3D capillaries versus the value of the adhesion parameter, $G_{ads,2}$, for different duct sizes [in Schaap's paper [13], G_c=0.025 and $G_{ads,2}$ between 0.0 and 0.020. Notice that, according to our definition in Eq. (5), G_c=0.9].

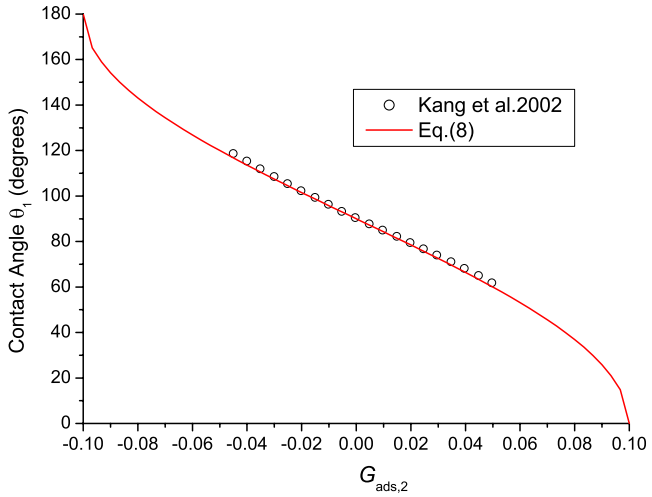

FIG. 8. (Color online) Dependence of the contact angle of the droplet θ_1, on the adhesion parameter $G_{ads,2}$ based on Kang *et al.* [7]. Other parameters are G_c=0.2 (in their paper, while according to our definition of cohesive force, here G_c=1.8), and $G_{ads,1}$=−$G_{ads,2}$.

Kang *et al.* [7] also carried out a study that empirically examined the dependency of the contact angle θ_1 on the interaction parameter $G_{ads,2}$ for 2D multicomponent fluids interacting with a surface. Although the contact angles in their study are limited to the range of 60° to 120°, these data are also useful to verify our method. The numerical results shown in Fig. 8 were digitized from [7]. We find that the numerical results agree very well with our simple formula again with only minor deviations (Fig. 8). It should be noted that, according to our definition of cohesive force [i.e., Eq. (5)], G_c equals 9 times the G_c defined by Kang *et al.* [7]. Hence, according to our definition, here G_c=1.8.

IV. CONCLUSION

In this paper, a method for determining the adhesion parameters that lead to an *a priori* fluid-solid contact angle in the Shan and Chen multicomponent, multiphase lattice Boltzmann model is proposed. To test the method, multicomponent fluids interacting with a surface were simulated. Our numerical results are consistent with the proposed formula based on Young's equation and given by Eq. (8). We evaluated the magnitude of deviation from Eq. (8) via a series of simulations and demonstrated a broad range of $G_{ads,1}$ and $G_{ads,2}$ parameter sets where the error is less than 2°. Our method was further verified by reevaluation of the previous numerical results of [13,7].

ACKNOWLEDGMENTS

Huang, Thorne, and Sukop were supported by the National Science Foundation under Grant No. 0440253. Schaap was supported, in part, by NSF-EAR-0337378 and NSF-EAR-061003.

[1] A. J. Briant, A. J. Wagner, and J. M. Yeomans, Phys. Rev. E **69**, 031602 (2004).
[2] T. Young, Philos. Trans. R. Soc. London **95**, 65 (1805).
[3] R. Finn, Phys. Fluids **18**, 047102 (2006).
[4] X. Shan and H. Chen, Phys. Rev. E **47**, 1815 (1993).
[5] P. Raiskinmäki, A. Koponen, J. Merikoski, and J. Timonen, Comput. Mater. Sci. **18**, 7 (2000).
[6] N. S. Martys and H. D. Chen, Phys. Rev. E **53**, 743 (1996).
[7] Q. J. Kang, D. X. Zhang, and S. Y. Chen, Phys. Fluids **14**, 3203 (2002).
[8] P. Raiskinmäki, A. Shakib-Manesh, A. Jäsberg, and A. Koponen, J. Stat. Phys. **107**, 143 (2002).
[9] C. Pan, M. Hilpert, and C. T. Miller, Water Resour. Res. **40**, W01501 (2004).
[10] A. G. Yiotis, J. Psihogios, M. E. Kainourgiakis, A. Papaioannou, and A. K. Stubos, Colloids Surf., A **300**(1-2), 35 (2007).
[11] M. Latva-Kokko and D. H. Rothman, Phys. Rev. E **72**, 046701 (2005).
[12] S. Hou, X. Shan, Q. Zou, G. D. Doolen, and W. E. Sol, J. Comput. Phys. **138**, 695 (1997).
[13] M. G. Schaap, M. L. Porter, B. S. B. Christensen, and D. Wildenschild, Water Resour. Res. (in press).
[14] Q. J. Kang, D. X. Zhang, and S. Y. Chen, J. Fluid Mech. **545**, 41 (2005).
[15] R. Benzi, L. Biferale, M. Sbragaglia, S. Succi, and F. Toschi, Phys. Rev. E **74**, 021509 (2006).
[16] M. C. Sukop and D. T. Thorne, *Lattice Boltzmann Modeling: An Introduction for Geoscientists and Engineers* (Springer, Heidelberg, Berlin, New York, 2006).
[17] A. W. Adamson and A. P. Gast, *Physical Chemistry of Surfaces*, 5th ed. (John Wiley & Sons, Inc., New York, 1997).
[18] X. Shan and G. Doolen, J. Stat. Phys. **81**, 379 (1995).